Corrosion Behaviour of Crystalline and Amorphous Forms of the Glass Forming Alloy Fe$_{43}$Cr$_{16}$Mo$_{16}$C$_{15}$B$_{10}$

M.S. Bakare; K.T. Voisey; K. Chokethawai; D.G. McCartney.

Materials, Mechanics and Structures Research Division,

Faculty of Engineering, University of Nottingham, UK. NG7 2RD.

Corresponding Author:

Katy.voisey@nottingham.ac.uk

Tel: +44 115 951 4139 Fax: +44 115 951 3800

1

Abstract

The corrosion behaviour of both crystalline and largely amorphous forms of the Fe-based glass forming alloy, $Fe_{43}Cr_{16}Mo_{16}C_{15}B_{10}$ alloy was investigated. Two different methods were used to induce transformation to the amorphous form of the alloy: laser melting and HVOF spraying. Both methods produced largely amorphous material, however the high brittleness of the alloy makes it susceptible to cracking during laser treatment, hence this technique is not suitable for largescale application. Potentiodynamic scanning showed that in 0.5M H_2SO_4 and 3.5% NaCl electrolytes both amorphous forms of the alloy had better corrosion resistance (lower current densities for -200 to +1000mV SCE) compared to the crystalline material. The laser treated material and HVOF coating performed similarly in 3.5% NaCl. In 0.5M H_2SO_4 the HVOF coating had a lower current density than the laser melted material for almost all of the potential range -300 to +1000mV SCE. The improved corrosion behaviour of the largely amorphous material is attributed to its homogeneity, and particularly to the elimination of the Mo-rich phase that underwent preferential corrosion in the crystalline form of the material.

1 **Introduction**

Fe-based metallic glasses are of interest since they have the potential to combine their high corrosion resistance, excellent magnetic properties and high strength with a commercially attractive low cost [1].

Fe-Cr-Mo-C-B alloys have been noted to have both good glass forming abilities and good corrosion resistance of the amorphous phase [2]. Huang et al. [3] report that fully amorphous ribbons of Fe-Cr-Mn-Mo-W-B-C-Si and Fe-Cr-Mn-W-B-C-Y have exceptional corrosion resistance in both acidified and neutral chloride solutions. Farmer et al. [4] examine the corrosion behaviour of a series of amorphous alloys based on $Fe_{52.3}Cr_{19}Mn_2Mo_{2.5}W_{1.7}B_{16}C_4Si_{2.5}$ and show that the corrosion resistance of these alloys can outperform that of wrought alloy 22 in seawater at temperatures up to 90ºC. Gostin et al. [5] have shown that the corrosion resistance of the amorphous form of $(Fe_{44.3}Cr_5Co_5Mo_{12.8}Mn_{11.2}C_{15.8}B_{5.9})_{98.55}Y_{1.5}$ is superior to that of the crystalline form in chloride solutions and in acid, though a pH dependence is noted with the amorphous structure being of no benefit in highly alkaline solutions.

However, the generally low ductility, combined with the difficulties of obtaining high enough cooling rates to produce large gauge glassy material, impede the use of metallic glasses as structural materials. A more viable way of exploiting these materials is as coatings. In thermal spraying high cooling rates of up to $\sim 10^8 Ks^{-1}$ can be achieved [6] as the molten and partially molten particles impact the substrate to build up the coating, making it a suitable process for the formation of coatings of glassy metallic alloys. High velocity oxy-fuel (HVOF) is of particular interest due to the decreased porosity and oxide contents produced compared to other thermal spray techniques [7]. Laser surface treatment is also well suited to the production of the amorphous phase due to the high cooling rates of up to 10^5 K s^{-1} produced [8].

Both processes have successfully produced amorphous coatings or surface layers. Hoekstra et al. [9] used excimer laser surface treatment to produce an amorphous-like surface on $Al_{94}Co_{7.5}Ce_{8.5}$, Audebert et al. [10] have generated amorphous phases in Zr- and Mg- based alloys, Carvalho et al. [11] used a two step laser process to generate an essentially amorphous coating of $Zr_{60}Al_{15}Ni_{25}$. It should be noted that the surfaces produced are usually referred to as largely or essentially amorphous, with some fraction of crystalline material present. The improvement in corrosion behaviour has been directly correlated to the proportion of amorphous material present [11].

Thermal spraying has been used to generate the amorphous phase in a number of types of glass forming alloys. Taileart et al. [12] have successfully used the pulsed thermal spray (PTS) technique to generate largely amorphous coatings of an Al-Co-Ce alloy. They report that the corrosion behaviour of the coatings approaches that of melt spun ribbons, i.e. a fully amorphous form, of a similar composition [12]. The presence of some nanocrystals is reported but does not significantly affect the corrosion behaviour of the, mainly amorphous, coatings [13]. Choi et al. [14] generated amorphous material using HVOF with an NiTiZrSiSn feedstock powder. Guo et al. [15] have used HVOF and HVAF to deposit partially amorphous coatings using a $Fe_{49.7}Cr_{18}Mn_{1.9}Mo_{7.4}W_{1.6}B_{15.2}C_{3.8}Si_{2.4}$ powder. Farmer et al. [4] used HVOF to deposit $Fe_{49.7}Cr_{17.7}Mn_{1.9}Mo_{7.4}W_{1.6}B_{15.2}C_{3.8}Si_{2.4}$ and $Fe_{48}Mo_{14}Cr_{15}Y_2C_{15}B_6$ coatings and report some dependency of corrosion behaviour on the

feedstock powder size. Zhou et al. [16,17] have created largely amorphous $Fe_{48}Cr_{15}Mo_{14}C_{15}B_6Y_2$ HVOF coatings with some nanocrystals present. Again, a good corrosion resistance in chloride solutions is reported as well as a decreased corrosion resistance in alkaline solutions [17].

However, neither process simply converts the surface into the amorphous phase. Laser treatment can result in crack formation as well as incomplete amorphisation [9,11]. An HVOF sprayed coating can be significantly different to the bulk material of the same composition as the spraying process can introduce porosity, oxides, regions of unmelted and resolidified material and a lamellar microstructure as well as producing the amorphous phase [18,19]. Such features are known to affect the corrosion behaviour [17] [18,20]. The superior corrosion resistance of metallic amorphous alloys is attributed to the lack of defects such as dislocations and grain boundaries which can act as sites of preferential attack in crystalline metals. Hence there is interest in relating corrosion behaviour to the microstructural details of these materials.

This paper reports the corrosion behaviour of the Fe-based glass forming alloy $Fe_{43}Cr_{16}Mo_{16}C_{15}B_{10}$ (initially developed in Inoue's group [21]) in both its crystalline and amorphous forms. In order to directly determine the effects of the microstructural modifications due to HVOF spraying on amorphous corrosion resistant coatings, two amorphous forms of the same alloy are studied: an HVOF sprayed coating and laser surface melted material. Corrosion testing is carried out using the potentiodynamic testing in 0.5M H_2SO_4 and 3.5 % NaCl. Samples are characterised by X-ray diffraction, differential scanning calorimetry and scanning electron microscopy.

2   Experimental Procedures

2.1   Materials and sample preparation

Table 1 presents the composition of the master alloys used for the production of the Fe-based bulk metallic glass alloy as received from BMI foundry services Ltd, Halesowen, UK. A total of 2.0 kg of material was melted in an induction furnace by heating to a temperature of around 1923 K before pouring into a mild steel mould of 305(l)x110(w)x60(h)mm that was pre-heated to ~150 C to form a flat casting of approximately 10 mm in thickness which cooled naturally.

Using a gas atomised $Fe_{43}Cr_{16}Mo_{16}C_{15}B_{10}$ powder, the coating was deposited unto a mild steel substrate (60 x 25 x 2 mm) by a metjet-II liquid fuel HVOF system [20]. For proper adherence of the coating to the mild steel substrate, degreasing and grit blasting of the substrate was carried out prior to deposition. The process spraying parameters used are shown in Table 2.

A 2 kW IPG YLR 2000S fibre laser with wavelength of 1070 nm and a 20.7 mm mrad beam product parameter was used to melt the as-cast bulk alloy for microstructural modification. The laser power and samples traverse speed chosen for this work are 1000 Watts and 1000 mm/min respectively. A 600 μm process fibre focussed 20 mm above the sample was used to create laser melted tracks of approximately 2 mm in width. To further ensure rapid cooling of the laser treated track, flowing air with pressure of 1.2 bar was used to cool the samples continuously during and immediately after melting.

4

2.2   Corrosion tests

The corrosion behaviour of these samples was assessed by potentiodynamic polarisation in 0.5M H_2SO_4 and 3.5 % NaCl at 30 $^{\circ}$C using a potentiostat from ACM instruments, Cumbria, UK. The experiment was set up using ASTM standard G5-94 with a three electrode cell: working electrode (WE), platinum counter electrode (AE) and reference calomel electrode (RE). For both as-cast bulk and coated samples, the surfaces were polished to 1 μm prior to testing with approximately 0.15 cm^2 area exposed to electrolyte. For the laser treated samples, only the fully treated track was exposed to the electrolytes also using the same area. In all experiments, the time interval between polishing and prior immersion in electrolytes was 2.5 hours. The deaeration of the electrolyte, achieved by bubbling nitrogen gas, was started 30 minutes prior to the experiment and continued until the end of the experiment. 1-hour open circuit stability was carried out before potentiodynamic polarisation. A 0.33 mV s^{-1} sweep rate was used. Passive current density (i_p) and the corrosion potential (E_{corr}) were used to interpret the corrosion behaviour of the samples. Reproducibility of data was ensured by repeating tests at least three times. Corrosion current density, i_o, values were determined by extrapolating the anodic and cathodic Tafel regions of the potentiodynamic results around E_{corr} with the intersection being reported as i_o.

2.3   Microstructural characterisation and thermal stability analysis

The particle size range, as determined by laser difractometry using a Malvern Mastersizer S, was -63 +15 μm, i.e. 10 vol % of the powder had a diameter exceeding 65 μm, and 10 vol % had a diameter less than 15 μm. The mean diameter, d50, was 31 μm. The samples were characterised using energy dispersive spectroscopy (EDS), scanning electron microscopy (SEM XL30) in both secondary electron (SE) and back scattered electron (BSE) mode, in terms of microstructural morphology and chemical composition. SEM observations were performed before and after potentiodynamic polarisation to 1600 mV (wrt SCE). The X-ray diffraction analysis (XRD) of the as-cast and coated samples was performed using Crkα radiation (D-500 X-ray diffractometer) while due to smaller spot required for the laser treated sample, CrKα radiation (D8 discover X-ray diffractometer) was used. Hardness of both as-cast and laser treated alloys was obtained using micro hardness tester with a 1000 g load. Thermal analysis including determination of glass transition temperature (T_g), onset of crystallisation temperature (T_x), supercooled liquid region (ΔT_x), melting temperature (T_m) and reduced glass transition temperature index (T_g/T_m) was carried out for all samples using a differential-temperature type differential scanning calorimeter (TA Instruments model SDT Q600). Using ~ 60 mg of samples, the experiment was performed under a purified argon gas environment with a flow rate of 100 ml min^{-1} and a heating rate of 20 K min^{-1} between 293 – 1673 K. Recrystallised alumina sample pans were used. Calibration of the temperature scale of the instrument was carried out by using the melting points of aluminium (933 K) and gold (1287 K).

Phase proportions and the total oxide plus porosity content were determined by image analysis. SEM micrographs of cross-sections were analysed using ImageJ software, greyscale ranges corresponding to the relevant features were set and the proportion of pixels in these ranges determined. This gave an area fraction of each feature, which is equal to the volume

fraction assuming that a representative cross-section has been examined. In each case at least five micrographs with magnifications between x2000 and x2500 were analysed.

In addition the overall composition of the material produced was determined by the London and Scandinavian Metallurgical Company Ltd using a combination ICP-IRIS, LECO and x-ray fluorescence techniques.

3   **Results**

3.1   Microstructural characterisation

3.1.1   *Structure of as-cast glass forming alloy*

The overall composition of the as-cast alloy is (at. %) Fe: 42.5 %, Cr: 16.1 %, Mo: 16.1 %, C: 14.0 %, B: 9.9 %, Si: 1.3 %, very similar to the target composition of $Fe_{43}Cr_{16}Mo_{16}C_{15}B_{10}$. The as-cast material has a hardness of 1307 ± 7 HV. Observations of cracks readily propagating from the laser treated region into and through the surrounding material showed the as-cast material to be brittle. The material readily separated into fragments by cracking without any plastic deformation.

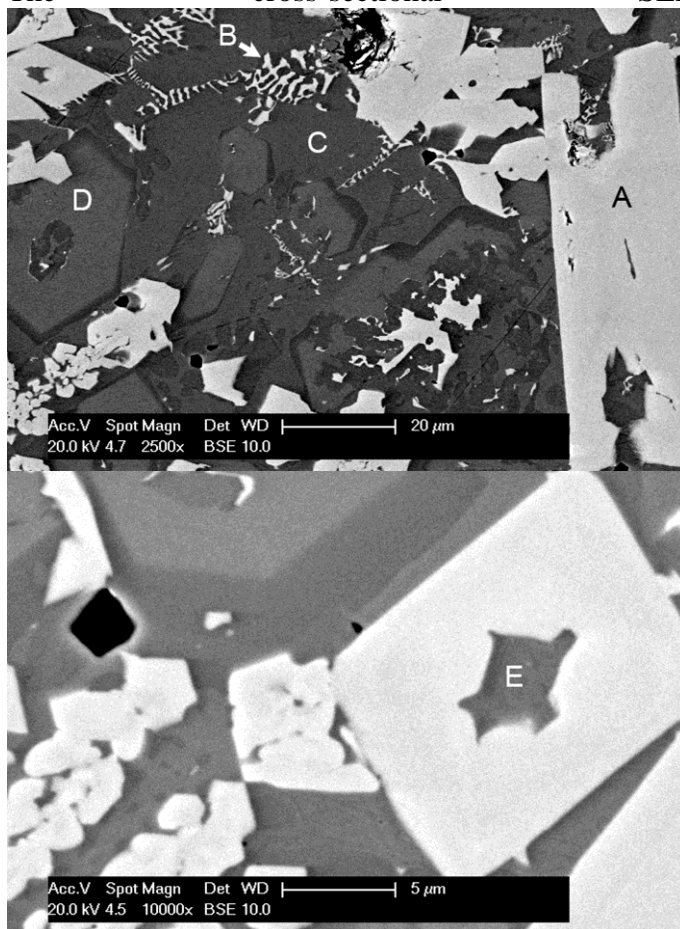The   cross-sectional   SEM   images   in

Figure 1 shows that the as-cast material has a multiphase microstructure. Five different phases, labelled A-E, are seen within the as-cast alloy. The large, blocky precipitates with the brightest contrast and ranging in size from ~10-100 μm are referred to as phase A. Also present are much smaller particles with a similar bright contrast, labelled as phase B. These form part of a eutectic intergrowth, and are typically 5 μm or less in size. Phase C is the dark phase that forms a matrix, with particles of the slightly darker contrast phase D embedded in it. The particles of phase D range up to ~ 30 μm in size. The fifth phase, E, is found as a darker contrast phase embedded within phase A.

EDS spot analysis (Table 3) results are used to compare the compositions of the different phases. It should be noted that due to the difficulty in obtaining reliable EDS results for C and B, only the metallic elements Fe, Mo and Cr are included in the analysis. The results show that both bright contrast phases (A & B) are enriched in Mo, the dark (C) and grey (D) phases have higher Fe and Cr contents. Image analysis revealed that the area fraction of bright phases is 41 ± 3 % in total, 22.3 ± 4 % for phase C and 36.7 ± 2 % for phase D.

XRD results show the as-cast glass forming alloy to be crystalline with Mo_2FeB_2, $M_{23}C_6$ and M_6C phases present, where M represents an unspecified metallic element.

By combining the SEM image, EDS and XRD results (Figure 2) together with reference to XRD results published for similar alloys [5,19], it is concluded that phase A is Mo_2FeB_2 while the tiny bright interdendritic phase B is M_3Mo_3C, where M represents (Fe,Cr) . The dark and grey areas (C and D) were both identified as $M_{23}(C,B)_6$ but with slightly different Mo and Fe contents, here M represents (Fe,Cr,Mo). Phase E
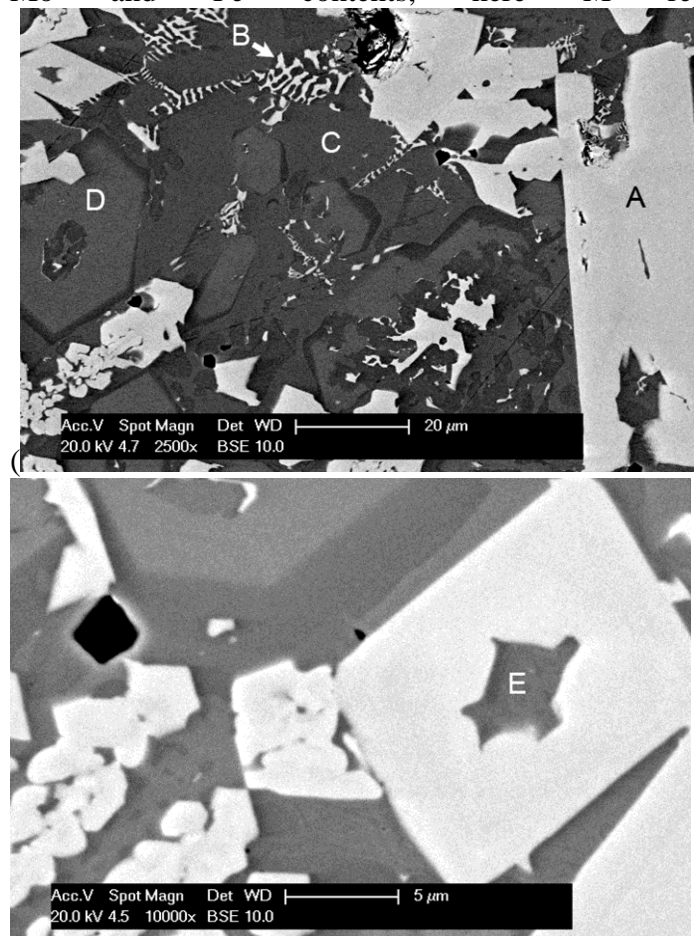
*Figure 1*b) was assigned as α-Fe due to the high Fe-content. The XRD results obtained are consistent with α-Fe being present. However, it should be noted that no XRD peaks unique to α-Fe were observed.

3.1.2 *Structure of as-cast bulk glass forming alloy after laser treatment*

After laser surface melting, a single laser track width ~2 mm was obtained. The laser treated track has a hardness of 1319±11 HV. EDS analysis was carried out to check if material composition had changed during laser treatment due to oxidation and/or evaporation processes. The EDS area composition results (Table 4) show a slight depletion in the Cr content of the laser treated track compared to the as-cast material. Cross-sectional SEM images of the track (Figure 4a) show a melt depth at the centre of the track of ~ 500 μm. There are two different zones present in the laser treated region (Figure 4ab): the completely homogenised region without any secondary phases and a heat-affected region containing 4 ± 0.2 vol% of the Mo_2FeB_2 precipitates. This heat affected region lies between the homogeneous track and untreated region. XRD of the homogenous region of the laser track revealed only broad/halo peaks around diffraction angles of $2\theta \sim 44°$ and $77°$ (Figure 2). No diffraction peaks corresponding to crystalline phases were seen, indicating that the laser treated alloy is at least largely amorphous. As is clearly seen in Figure 3a, laser melting resulted in cracking of the resolidified amorphous material.

3.1.3 *Structure of HVOF coating*

SEM examination of the as-received gas-atomised powder showed powder particles that were largely spherical or near-spherical in shape (Figure 4). There was no variation in contrast seen in cross-sectioned particles, indicating a uniform single phase. XRD analysis (Figure 2) confirmed that the powder was at least largely amorphous with a broad halo-peak at $2\theta \sim 35$-$55°$ and a second halo-peak at around $75°$.

Figure 5a shows the back scattered SEM image of a cross-section of the HVOF as-sprayed coating. The thickness of the coating is around 350-400 μm with an irregular top surface. EDS area analysis showed that the overall composition is (at%) 22% Cr, 55 % Fe and 23 % Mo (excluding C, B and O).

XRD results (Figure 2) confirmed the largely amorphous nature of the coating. Minor XRD peaks from an oxide phase were detected at $2\theta = 30°$, $35.7°$ and $62.8°$ (Figure 2b). The oxide formed was determined to be chromite, $FeCr_2O_4$.

The microstructure is typical of a thermally sprayed coating and consists of lamellarlike splats where successive layers of molten particles have spread out on impact and resolidified. Distinct, near-spherical, splats that arise from partially melted particles are also seen, again this is a common feature of a thermally sprayed coating (Figure 5b). Figure 5c is a higher magnification back scattered SEM image showing details of an area including both a fully melted region (F) and a partially melted particle (P). The EDS spectra and line scan of Mo, Fe, Cr and O, in the F and P regions showed an increase in the Mo signal to 500 counts compared to an average value of 400 counts that corresponded to the bright interlayer features seen in Figure 5c. The darker contrast areas were enriched in oxygen and are

attributed to be the $FeCr_2O_4$ oxide phase detected by XRD. Image analysis of SEM images determined that the combined porosity and oxide content is less than 5 vol%.

3.1.4 *Differential Scanning Calorimetry (DSC) analysis*

DSC traces for the powder, coating, laser treated and crystalline bulk alloy are shown in Figure 6 with key data summarised in Table 5. The glass transition temperature, T_g, is ~886-889 K while the onset of crystallisation temperature, T_x, is 957-960 K. All three samples have a similar supercooled liquid region, $\Delta T_x = T_x - T_g$, of 71-72 K and a similar reduced glass transition temperature index, T_g/T_m where T_m is the melting temperature, of 0.63. In each case the main crystallisation peak temperature, T_p, is at ~970-971 K. A smaller secondary crystallisation peak around 1143 K is also seen.

3.2 Potentiodynamic test

Anodic polarisation curves representative of repeated experiments of the as-cast, laser treated bulk alloy and HVOF sprayed coating in 0.5M H_2SO_4 are shown in Figure 7. In 0.5M H_2SO_4, the corrosion potential for crystalline material is -364±2 mV while that of laser treated amorphous alloy is -419±2 mV. The E_{corr} of the amorphous coating is -388±10 mV. Both amorphous forms have slightly lower corrosion potentials (E_{corr}) than the as-cast crystalline alloy. It is seen that both forms of the alloy largely consisting of amorphous material have lower current densities than the crystalline alloy (Table 6). The largely amorphous HVOF coating has lower current densities, i.e. better corrosion resistance, compared to the laser treated material. Corrosion current density, i_o, values for both the laser treated and HVOF sprayed samples are approximately 0.4 and 0.3 mA cm^{-2} respectively, an order of magnitude of the value for the crystalline material where i_o is about 2.5 mA cm^{-2}. The double steps seen in all polarisation curves in Figure 7 have also been observed by previous authors for a similar Fe-based glass forming alloy [17].

In 3.5 % NaCl solution, the amorphous forms of the glass forming alloy again showed better corrosion resistance compared to the the crystalline material, i.e. lower current densities (Figure 8). In this electrolyte the coating and laser treated amorphous alloy had very similar results. Compared to the results from the acid, corrosion potentials were less noble: -554±10 mV for laser treated bulk alloy and -546±64 mV for the largely amorphous coating. Details of the corrosion parameters are given in Table 6. Corrosion current density, i_o, values for all samples are of the same magnitude, being 0.02, 0.01 and 0.03 mA cm^{-1} for the crystalline, HVOF coating and laser treated samples respectively.

3.3 Samples after exposure

No large scale pitting events were seen on any of the samples tested. For the crystalline bulk alloy, SEM images of representative regions before and after potentiodynamic exposure to 0.5M H_2SO_4 (Figure 9) clearly show sites where preferential dissolution of the Mo-rich phases has occurred.

Figure 10 shows a region of the amorphous coating before and after polarisation in acid. Preferential corrosion of the resolidified regions around individual splats is seen.

Back scattered SEM images of the laser treated alloy before corrosion and after corrosion testing in acid are shown in Figure 11. For this sample the corrosion attack is in the form of small pit-like features uniformly distributed across the surface material. No increase in the extent of corrosive attack is seen in the immediate vicinity of the cracks.

4   **Discussion**

4.1.1   *Microstructure*

The target glass forming alloy was generated, the composition of the as-cast alloy is in line with that aimed for. The presence of ~0.7% Si is attributed to the presence of trace Si impurities in the starting master alloys. The as-cast material is crystalline with a complex microstructure consisting of four main phases. As previously observed in similar alloys [5,22], the matrix phase is $M_{23}C_6$, however, in this work two $M_{23}C_6$ phases with slightly different Mo and Fe contents form the matrix. Precipitates of Mo_2FeB_2 and M_3Mo_3C are also seen. This is similar to previous observations on a similar alloy [5]. The specific M_3Mo_3C phase present cannot be conclusively identified here. The small size of the particles present here does not aid their identification since it is possible that the signals collected by EDS come from a volume which extends beyond the particle of interest. However, there may not be a single composition of this phase present, as detailed in Sourmail's review [23] there is a large range of possible compositions for M_3MoC: both Fe_3Mo_3C and $(FeCr)_{21}Mo_3C_6$ have been reported. We have identified phase E as α-Fe, this is consistent with our XRD and EDS results. However, no unique XRD peaks were observed for this phase so further investigation is required to confirm its presence. The high hardness and extreme brittleness of the as-cast alloy is attributed to the presence of borides and carbides, as has been previously suggested [24]. DSC results in Table 5 are consistent with values previously reported for a similar alloy [21].

Laser surface melting successfully transformed the crystalline as-cast material, producing an at least largely amorphous form. However, the thermal stresses generated by laser treatment, combined with the highly brittle nature of the glass forming alloy resulted in cracking of the laser treated area. The generation of cracking is a frequent result of laser surface treatment [9]. There was concern that the heating cycles due to successive tracks could induce recrystallisation of neighbouring laser amorphised regions, laser treatment was therefore restricted to single tracks.

HVOF spraying of amorphous gas atomised powder particles of the alloy produced coatings in which the amorphous form of the alloy was at least largely retained. The coating produced is dense with the low amounts of porosity and oxides that are characteristic features of HVOF coatings [25]. The oxide detected in the coating results from partial oxidation during the deposition process, this may be minimised by further optimisation of spraying parameters. During sample preparation it was noted that some particles were detaching from the coating, i.e. there was some cohesive failure of the coating. This is attributed to the inherently high hardness and yield strength of the material inhibiting deformation of partially melted particles on impact, resulting in decreased coating cohesion. It has been shown that the amorphous

10

state has been largely retained even though melting and resolidification occurs during the HVOF process. Further optimisation of spraying parameters to increase the extent of melting, and thereby improve coating cohesion, is required. It should be noted that, as previously reported for similar materials, some nanocrystals are likely to be present in the amorphous forms of the material, however these were not directly observed in this work [16,17]. It has been suggested that such nanocrystals contribute to the good corrosion resistance of otherwise amorphous material [26].

4.1.2 *Corrosion*

Preferential dissolution of the Mo_2FeB_2 phase is clearly the mechanism of corrosion of the as-cast crystalline material in acidic medium. This indicates that the main matrix is more noble than Mo_2FeB_2, hence permitting the formation of galvanic cells. Amorphisation of the glass forming alloy eliminates the Mo_2FeB_2 precipitates and this mechanism of corrosion, resulting in better corrosion resistance of the largely amorphous material compared to the crystalline form.

Of the two largely amorphous forms of the glass forming alloy tested, the HVOF coating had better corrosion resistance than the laser treated material. This may be related to the cracks in the laser treated material. While no preferential attack was seen in the region of the cracks, the presence of the cracks will increase the effective surface area exposed to the electrolyte. This will, in turn, increase the apparent current density. EDS results suggest that laser treatment may produce a slight decrease in the Cr content: 17.4wt% Cr was detected in the laser treated material as opposed to 17.7wt% in the HVOF coating. It should be noted that EDS is not capable of accurately determining such small compositional differences. The corrosion resistance of the glass forming alloy is due to the Cr content, however any such minor difference in composition is not believed to significantly contribute to the slightly better corrosion performance of the HVOF coating compared to the laser treated material.

Preferential corrosive attack of the splat boundary regions was seen in the HVOF coating. This may be due to localised compositional variations. Previous work has shown that even minor localised variations in composition can degrade corrosion resistance [18]. Further analysis of the HVOF coatings is required to determine any such variation in this material. The laser treated material corroded via the formation of small pit like features. This work has not been able to correlate the location of these pits with any specific microstructural features.

The corrosion results presented in Table 6 generally show greater proportional variation for the HVOF coating than for the other samples. This is attributed to the inherent sample to sample variation in sprayed coatings, resulting from the porosity and oxides present. The i_o values seen in this work for the largely amorphous forms of the alloy in the acidic electrolyte are two orders of magnitude greater than the i_o values of approximately 10^{-1} mA cm^{-2} that can be determined from results previously reported by Pang et al. for a similar material, albeit in a more aggressive environment, 6 N HCl [2]. Results from Farmer et al. [4] for a melt spun version of a similar alloy in seawater show i_o to be approximately 10^{-2} mA cm^{-2}, three orders of magnitude less than that seen in this work. It should be noted that there is a relatively large error associated with these results due to the shape of the potentiodynamic curves. However, this source of error does not fully explain the difference in magnitude between our results and those reported elsewhere. The reproducibility of the results presented here has been checked by multiple runs of the experiments. It is possible that the i_o values are sensitive to the sample

preparation carried out; surfaces were polished to 1 μm prior to testing. Farmer et al. [4] do not mention any surface preparation of their samples prior to corrosion testing, Pang et al.[2] only state that surfaces were degreased. The same experimental equipment and procedure has previously produced i_o values of ~10^{-3} and 10^{-2} mA cm^{-2} for Inconel 625 in 0.5M H$_2$SO$_4$ and 3.5% NaCl respectively [18, 20]. Similar results for Inconel 625 in 3.5% NaCl have been reported by Zhang et al. [29] who used a similar sample preparation procedure to that used here: they ground to 1500 grit SiC. It is known that sample preparation can effect corrosion behaviour by generating an increased dislocation density, and hence a greater density of fast diffusion paths, in the near surface region [30]. While such a dislocation based mechanism is unlikely to be active in the largely amorphous material used here, the possibility of an analogous sample preparation related mechanism warrants further investigation.

Overall, the better corrosion resistance of the mainly amorphous form of the glass forming alloy, compared to the crystalline material, is attributed to the formation of a homogeneous single-phase solid solution [21,25,26]. The absence of surface heterogeneities such as segregation, dislocations, inclusions, grain boundaries as well as second phase precipitates, will not only reduce the possibility of galvanic cells and nucleation sites for corrosion but is also expected to enhance the stability of the passive films by decreasing the number of features that may result in passive film defects.

Laser treatment can generate the amorphous form of the alloy, however the usefulness of this technique is limited by the cracking it generates. HVOF spraying has successfully deposited glass forming alloy coatings that largely retain the amorphous state. With further optimisation of spraying conditions this method could be used to produce amorphous glass forming alloy coatings for corrosion protection applications.

Conclusions

- A glass forming alloy, Fe$_{43}$Cr$_{16}$Mo$_{16}$C$_{15}$B$_{10}$, has been formed which comprises of five phases: two M$_{23}$C$_6$ phases, Mo$_2$FeB$_2$, M$_3$Mo$_3$C (where M = Fe, Cr) and small amounts of α-Fe.

- The amorphous form of Fe$_{43}$Cr$_{16}$Mo$_{16}$C$_{15}$B$_{10}$ has been shown to have better corrosion resistance compared to the crystalline form in both 0.5M H$_2$SO$_4$ and 3.5% NaCl.

- Corrosion of the crystalline form is by preferential dissolution of Mo-rich precipitates.

- The improved corrosion behaviour is attributed to the homogeneity of the amorphous material.

- Conversion of the crystalline as-cast form of the alloy to the amorphous form by laser surface melting has been demonstrated. However, the usefulness of laser surface melting as a method to amorphise the alloy is limited by cracking of the brittle alloy due to thermal stresses.

- The difference in corrosion performance of the two different amorphous forms of the alloy is attributed to the very different microstructures.

- HVOF can deposit amorphous $Fe_{43}Cr_{16}Mo_{16}C_{15}B_{10}$ coatings that retain the amorphous structure, however further optimisation of HVOF spraying parameters is required.

References

[1]Liu, F., Q. Yang, S. Pang and T. Zhang: Effect of Mo element on the properties of Fe–Mo–P–C–B bulk metallic glasses Journal of Non-Crystalline Solids(2009) 355, 1444-1447.

[2]Pang, S. J., T. Zhang, K. Asami and A. Inoue: Bulk glassy Fe–Cr–Mo–C–B alloys with high corrosion resistance. Corrosion Science(2002) 44, 1847–1856.

[3]Huang, R., D. J. Horton, F. Bocher and J. R. Scully: Localized Corrosion Resistance of Fe-Cr-Mo-W-B-C Bulk Metallic Glasses Containing Mn+Si or Y in Neutral and Acidified Chloride Solutions. Corrosion(2010) 66, Article number: 035003.

[4]Farmer, J., J.-S. Choi, C. Saw, J. Haslam, D. Day, P. Hailey, T. G. Lian, R. Rebak, J. Perepezko, J. Payer, D. Branagan, B. Beardsley, A. D'amato and L. Aprigliano: Iron-Based Amorphous Metals: High-Performance Corrosion-Resistant Material Development. Metallurgical and Materials Transactions A(2009) 40A, 1289-1305.

[5]Gostin, P. F., A. Gebert and L. Schultz: Comparison of the corrosion of bulk amorphous steel with conventional steel. Corrosion Science(2010) 52, 273-281.

[6]Moreau, C., P. Cielo, M. Lamontagne, S. Dallaire, J. C. Krapez and M. Vardelle: Temperature evolution of plasma-sprayed niobium particles impacting on a substrate. Surface & Coatings Technology(1991) 46, 173-187.

[7]Helali, M. M. and M. S. J. Hashmi (1992). A comparative study of plasma spraying and high velocity oxy-fuel (HVOF) thermal spraying. 10th Conference of the Irish Manufacturing Committee (IMC 10). Galway, Ireland: 377-387.

[8]Hofmeister, W., M. Griffith, M. Ensz and J. Smugeresky: Solidification in direct metal deposition by LENS processing. Jom-Journal of the Minerals Metals & Materials Society(2001) 53, 30-34.

[9]Hoekstra, J. G., S. B. Qadri, J. R. Scully and J. M. Fitz-Gerald: Laser surface modification of a crystalline Al-Co-Ce alloy for enhanced corrosion resistance. Advanced Engineering Materials(2005) 7, 805-809.

[10]Audebert, F., R. Colaco, R. Vilar and H. Sirkin: Production of glassy metallic layers by laser surface treatment. Scripta Materialia(2003) 48, 281-286.

[11]Carvalho, D., S. Cardoso and R. Vilar: Amorphisation of Zr60Al15Ni25 surface layers by laser processing for corrosion resistance. Scripta Materialia(1997) 37, 523-527.

[12]Tailleart, N., B. Gauthier, S. Eidelman and J. R. Scully: Metallurgical and Physical Factors in Improving the Corrosion Resistance of Thermally Sprayed Semi-Amorphous Al-Co-Ce Coatings. ECS Transactions(2009) 16, 39-63.

[13]Presuel-Moreno, F., M. A. Jakab, N. Tailleart, M. Goldman and J. R. Scully: Corrosion-resistant metallic coatings. Materials Today(2008) 11, 14-23.

[14]Choi, H. S., S. H. Yoon, G. Y. Kim, H. H. Jo and C. H. Lee: Phase evolutions of bulk amorphous NiTiZrSiSn feedstock during thermal and kinetic spraying processes. Scripta Materialia(2005) 53, 125-130.

[15]Guo, R. Q., C. Zhang, Q. Chen, Y. Yang, N. Li and L. Liu: Study of structure and corrosion resistance of Fe-based amorphous coatings prepared by HVAF and HVOF. Corrosion Science(2011) 53, 2351-2356.

[16]Zhou, Z., L. Wang, D. He, F. Wang and Y. Liu: Microstructure and Wear Resistance of Fe-Based Amorphous Metallic Coatings Prepared by HVOF Thermal Spraying. Journal of Thermal Spray Technology(2010) 19, 1287-1293.

[17]Zhou, Z., L. Wang, F. C. Wang, H. F. Zhang, Y. B. Liu and S. H. Xu: Formation and corrosion behavior of Fe-based amorphous metallic coatings by HVOF thermal spraying. Surface and Coatings Technology(2009) 204, 563-570.

[18]Ahmed, N., M. S. Bakare, D. G. McCartney and K. T. Voisey: The effects of microstructural features on the performance gap in corrosion resistance between bulk and HVOF sprayed Inconel 625. Surf Coat Tech(2010) 204, 2294-2301.

[19]Chokethawai, K., D. G. McCartney and P. H. Shipway: Microstructure evolution and thermal stability of an Fe-based amorphous alloy powder and thermally sprayed coatings. Journal of Alloys and Compounds(2009) 480, 351-359.

[20]Zhang, D., S. J. Harris and D. G. McCartney: Microstructure Formation and Corrosion Behaviour in HVOF-Sprayed Inconel 625 Coatings. Mat Sci Eng A(2003) 344, 45-56.

[21]Pang, S. J., T. Zhang, K. Asami and A. Inoue: Synthesis of Fe-Cr-Mo-C-B-P bulk metallic glasses with high corrosion resistance. Acta Materialia(2002) 50, 489-497.

[22]Iqbal, M., J. I. Akhter, H. F. Zhang and Z. Q. Hu: Synthesis and characterization of bulk amorphous steels. Journal of Non-Crystalline Solids(2008) 354, 3284-3290.

[23]Sourmail, T.: Precipitation in creep resistant austenitic stainless steels. Mat Sci Tech (2001) 17, 1-14.

[24]Yu, H., Y. Zheng, W. Liu, X. pang, J. Zheng and W. Xiong: Effect of Mo/B atomic ratio on the microstructure and mechanical properties of Mo_2FeB_2 based cermets. International Journal of Refractory Metals & Hard Materials.(2010).

[25]Edris, H., D. G. McCartney and A. J. Sturgeon: Microstructural characterization of high velocity oxy-fuel sprayed coatings of Inconel 625. Journal of Materials Science(1997) 32, 863-872.

[26]Johnson, W. C., P. Zhou, A. M. Lucente and J. R. Scully: Composition Profiles around Solute-Lean, Spherical Nanocrystalline Precipitates in an Amorphous Matrix: Implications for Corrosion Resistance. Metallurgical and Materials Transactions A(2009) 40, 757-767.

[27]Wang, S. L., H. X. Li, X. F. Zhang and S. Yi: Effects of Cr contents in Fe-based bulk metallic glasses on the glass forming ability and the corrosion resistance. Materials Chemistry and Physics(2009) 113, 878-883.

[28]Wang, W. F., M. C. Wang, Z. Jie, F. Sun and D. Huang: Research on the microstructure and wear resistance of titanium alloy structural members repaired by laser cladding. Optics and Lasers in Engineering(2008) 46, 810-816.

[29]Zhang, T., H. Jing, Y. Han and L. Xu: Electrochemical behavior of corrosion resistance alloys. Mat Pro Tech(2012) 418-420, 1097-1101.

[30]Ostwald, C., H.J. Grabke: Initial oxidation and chromium diffusion. I. Effects of surface working on 9–20% Cr steels. Corros Sci(2004) 46, 1113-1127.

Tables

Table 1: Composition of master alloys (raw materials) for casting (weight percentage)

Master alloy	Fe	C	Si	S	P	Cr	Mo	Cu	Al	B	Ash	Moisture
Fe-C-Cr	Bal.	8.0	0.32	0.055	0.022	65.3	-	-	-	-	-	-
Fe-B	Bal.	0.19	0.42	0.002	0.027	-	-	-	0.11	18.2	-	-
Fe-Mo	Bal	0.01	1.30	0.04	0.04	-	68.5	0.51	-	-	-	-
C (Graphite)	-	99.0	-	0.05	-	-	-	-	-	-	<1.00	0.50
Mild steel	98.6	0.11	0.20	0.02	<0.01	0.10	<0.01	0.14				

Table 2: HVOF spraying process parameters using Metjet-II gun type.

Oxygen flow rate (l/min)	Fuel flow rate (l/min)	Nitrogen flow rate (l/min)	Nozzle length (mm)	Spray distance (mm)
915	0.33	7.0	100	355

Table 3: Percentage elemental composition of different phases in crystalline alloy (weight %)

	Large bright (A)	Tiny bright (B)	Dark (C)	Grey (D)	(E)
Cr	10.3	7.4	36.3	34.2	13.6
Fe	17.6	34.6	44.8	36.6	76.3
Mo	72.4	57.9	18.9	29.2	10.1
Possible identity	$Mo_2(Fe,Cr)B_2$	$(Fe,Cr)_3Mo_3(C,B)$	$M_{23}(C,B)_6$ M-(Fe, Cr, Mo)	$M_{23}(C,B)_6$ M-(Fe, Cr, Mo)	α-Fe

Table 4: Showing EDS wt.% composition of both crystalline (untreated) and amorphous region in Figure 3b

	Crystalline	Amorphous
Cr	19.6	17.4
Fe	48.2	49.8
Mo	32.2	32.8

Table 5: Details of DSC analysis of amorphous powder, coating and laser treated bulk alloy.

Sample	T_g (K)	T_x (K)	ΔT_x (K)	T_m (K)	T_g/T_m	T_p (K)
Powder	889	960	71	1406	0.63	971
Coating	886	957	71	1408	0.63	970
Laser treated	888	960	72	1414	0.63	971

Table 6: Corrosion potentials (E_{corr}) and current densities at various potentials.

	E_{corr} (mV)	i_o (mAcm^{-2})	i@0 mV (mAcm^{-2})	i@500 mV (mAcm^{-2})	i@1000 mV (mAcm^{-2})
Crystalline bulk (H$_2$SO$_4$)	-364±2	2.5±0.5	10.1±3.8	96.1±9.1	74.1±7.4
Amorphous coating (H$_2$SO$_4$)	-388±10	0.3±0.05	0.5±0.01	4.0±0.6	23.0±4.0
Laser treated bulk (H$_2$SO$_4$)	-419±2	0.4±0.05	2.2±0.2	10.1±0.8	15.4±1.5
Crystalline bulk (NaCl)	-622±30	0.02±0.005	26.4±3.8	14.1±2.1	189.3±14.9
Amorphous coating (NaCl)	-546±64	0.01±0.005	0.5±0.3	1.0±0.5	8.5±0.3
Laser treated bulk (NaCl)	-554±10	0.03±0.005	0.5±0.1	1.5±0.1	10.6±2.3
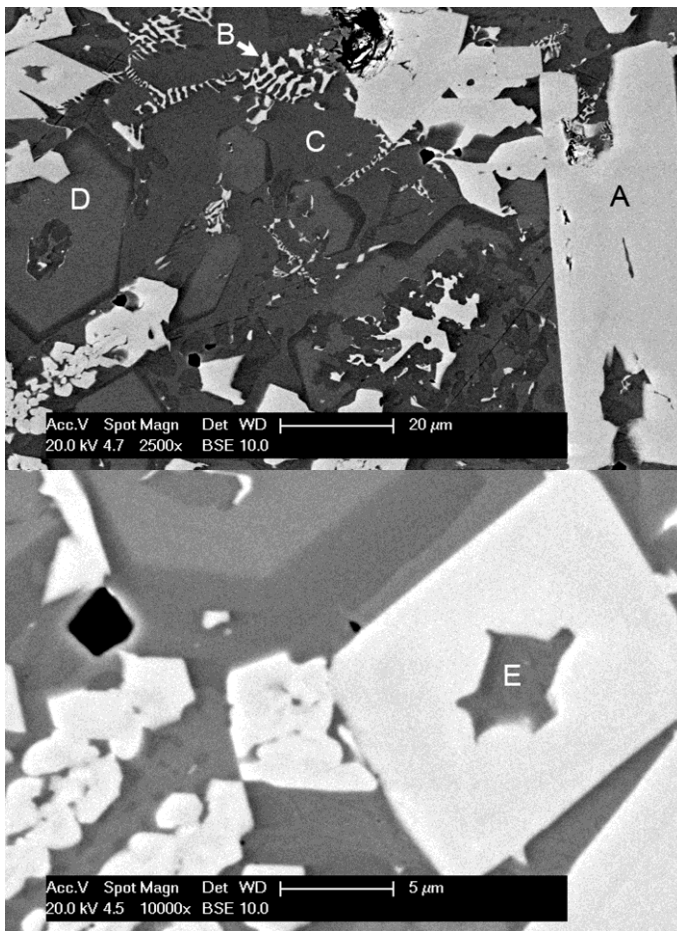
Figure 1: Back scattered SEM image showing a plan view of the as-cast glass forming alloy (a) Four different phases (A-D) are labelled; (b) Higher magnification image showing a fifth phase (E).
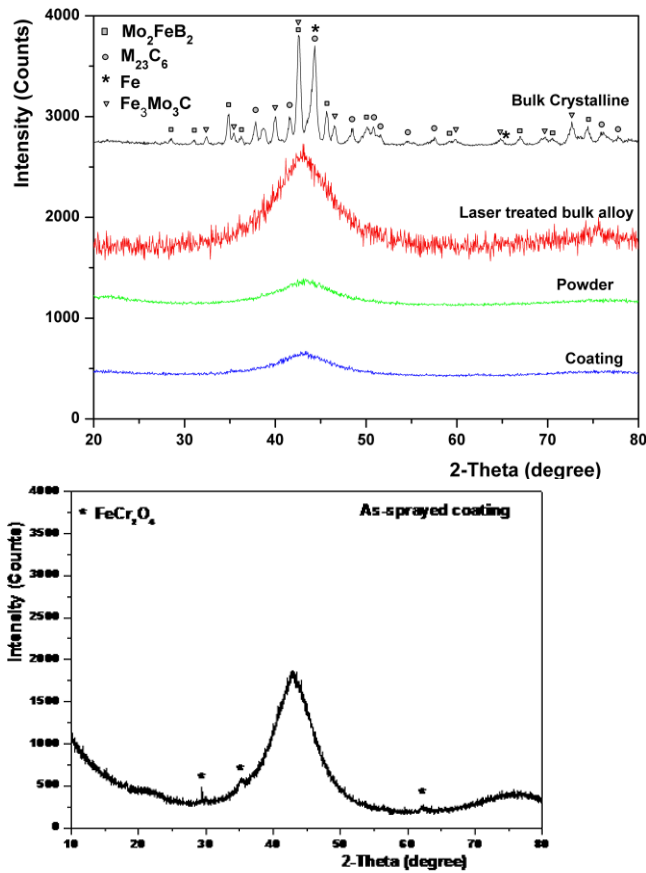
Figure 2: (a) Comparison of XRD scans of $Fe_{43}Cr_{16}Mo_{16}C_{15}B_{10}$ (at %) alloy showing peaks of different phases in the crystalline glass forming alloy and halo peaks in amorphous laser treated bulk alloy and coating, (b) Oxide peaks detected for the HVOF coating.
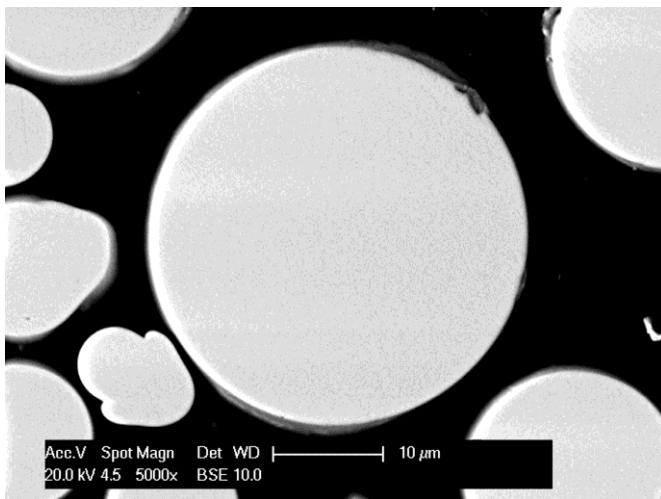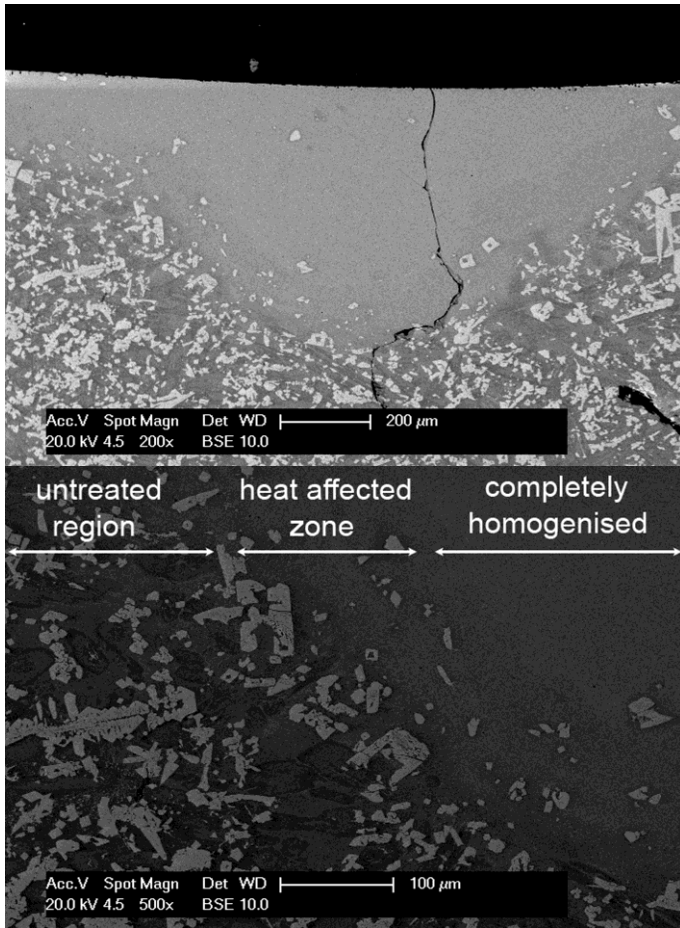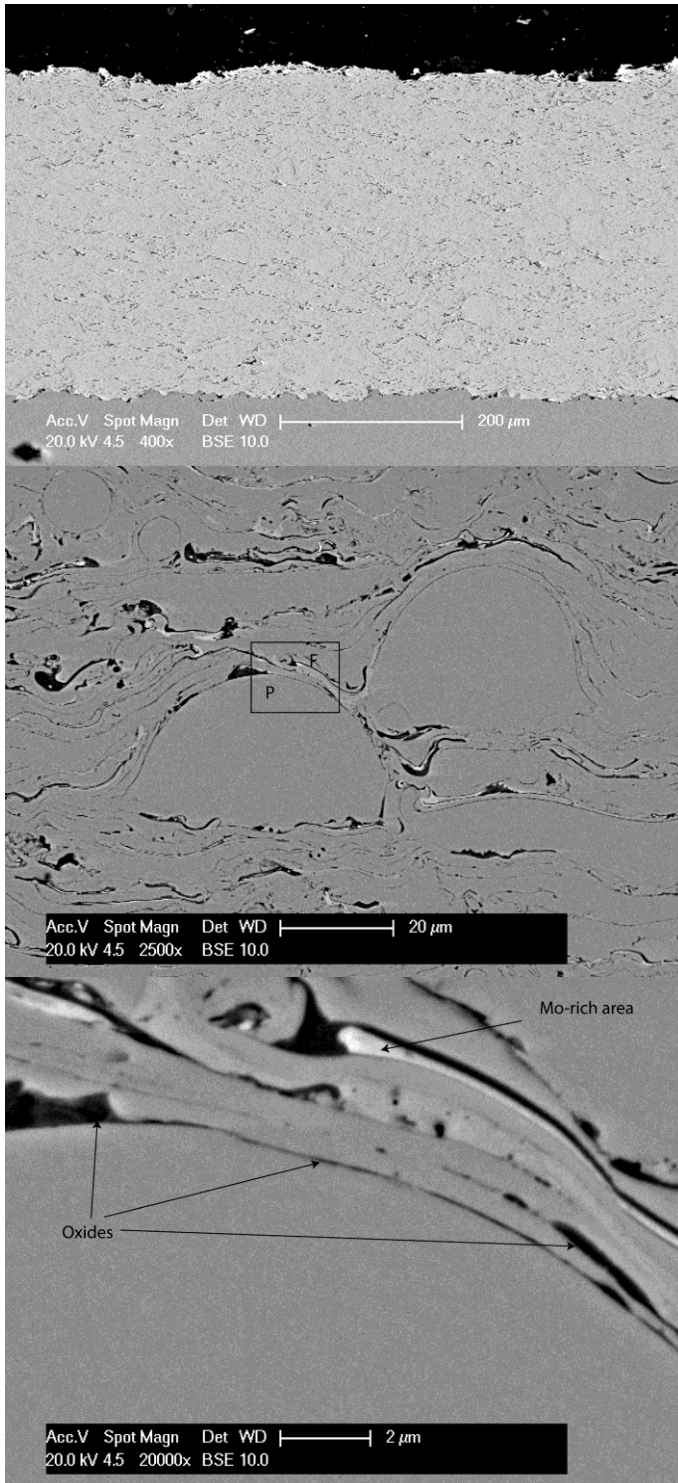

Figure 3: Cross-sectional view and magnified view of amorphous GF alloy formed using fiber laser (a) thickness of the laser treated amorphous area (b) different regions after laser treatment.

19

Figure 4: Back scattered SEM image showing a cross-section of the HVOF feedstock powder.

Figure 5: SEM images of cross-sections of Fe$_{43}$Cr$_{16}$Mo$_{16}$C$_{15}$B$_{10}$ (at%) coated samples (a) full thickness of the coating (b) splat morphology and regions of fully and partially melted material (c) higher magnification of region in the box in b, showing an Mo-rich area and oxides.

21
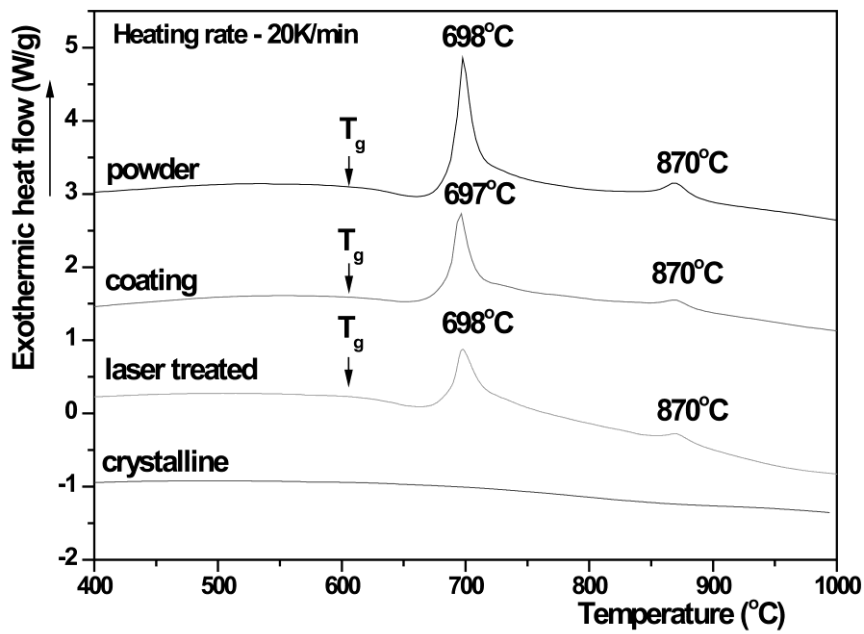
*Figure 6: DSC traces for powder, coating, laser treated and crystalline bulk forms of the alloy.*
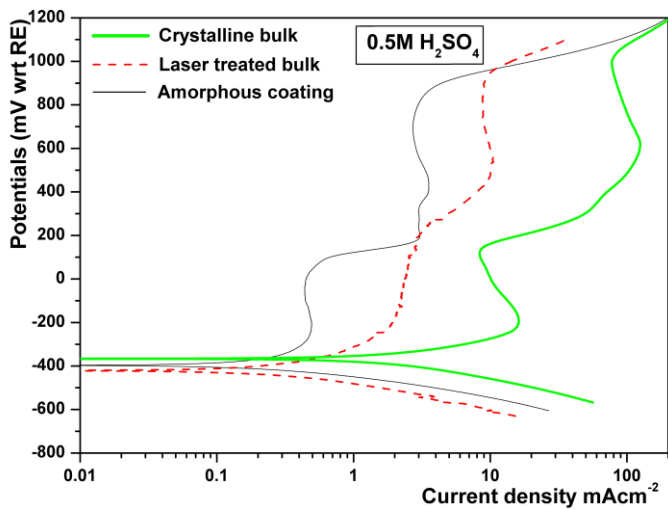
Figure 7: Potentiodynamic polarisation curves of crystalline glass forming alloy, amorphous GF bulk alloy and amorphous coating Fe-Cr-Mo-C-B in 0.5 M H_2SO_4
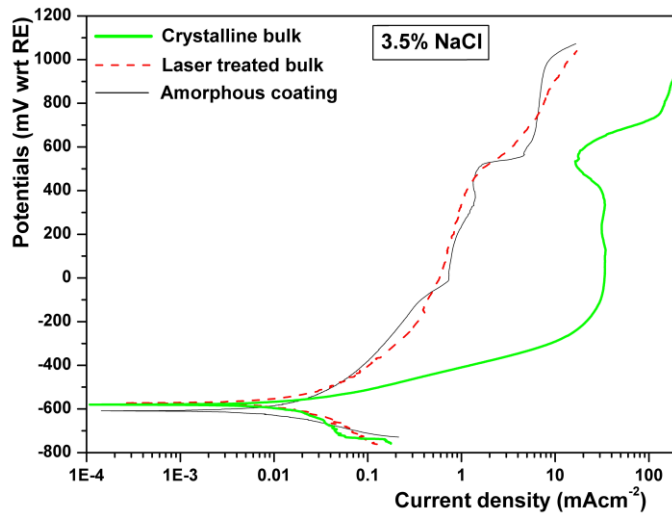
Figure 8: Potentiodynamic polarisation curves of both crystalline bulk amorphous glass forming alloy and amorphous coating of Fe-Cr-Mo-C-B in 3.5 % NaCl
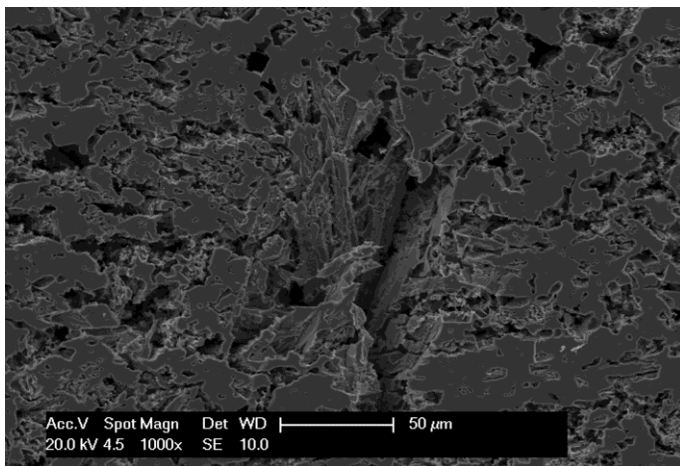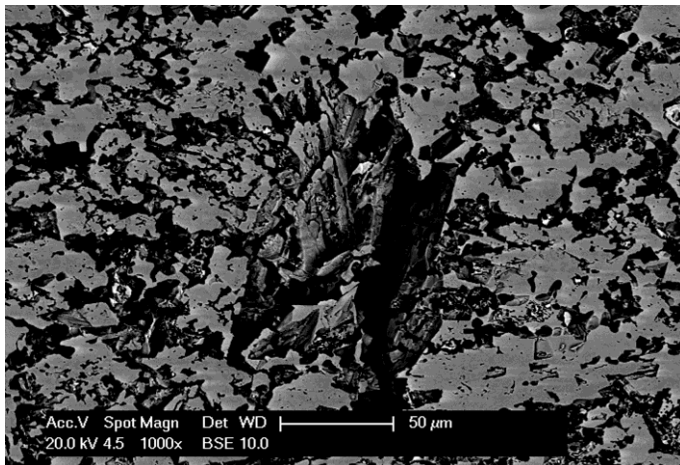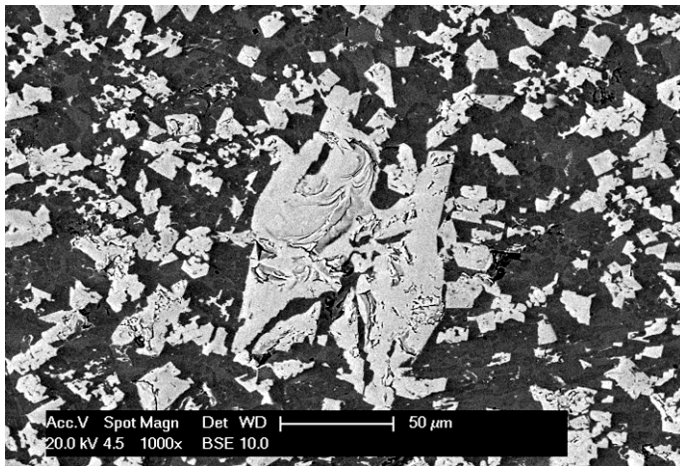
Figure 9: Surface morphology of bulk crystalline alloy before and after polarisation. (a) BSE image corrosion test (b) BSE image of the same area of the sample after corrosion test showing preferential dissolution of the Mo_2FeB_2 (large bright) phase (c) SE image showing preferential dissolution of the Mo_2FeB_2 phase.

24
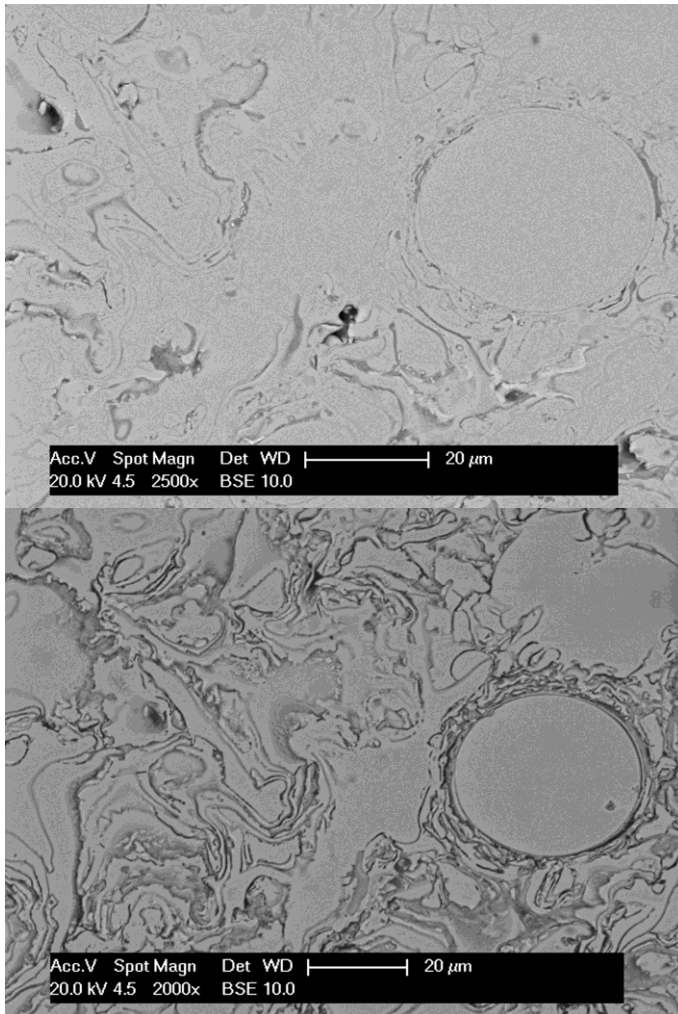
Figure 10: Surface morphology of amorphous sprayed coating samples before and after polarisation in BSE mode (a) before corrosion (b) after polarisation in 0.5M H_2SO_4 showing clearly the origin of corrosion at the melted and resolidified region around the splat.
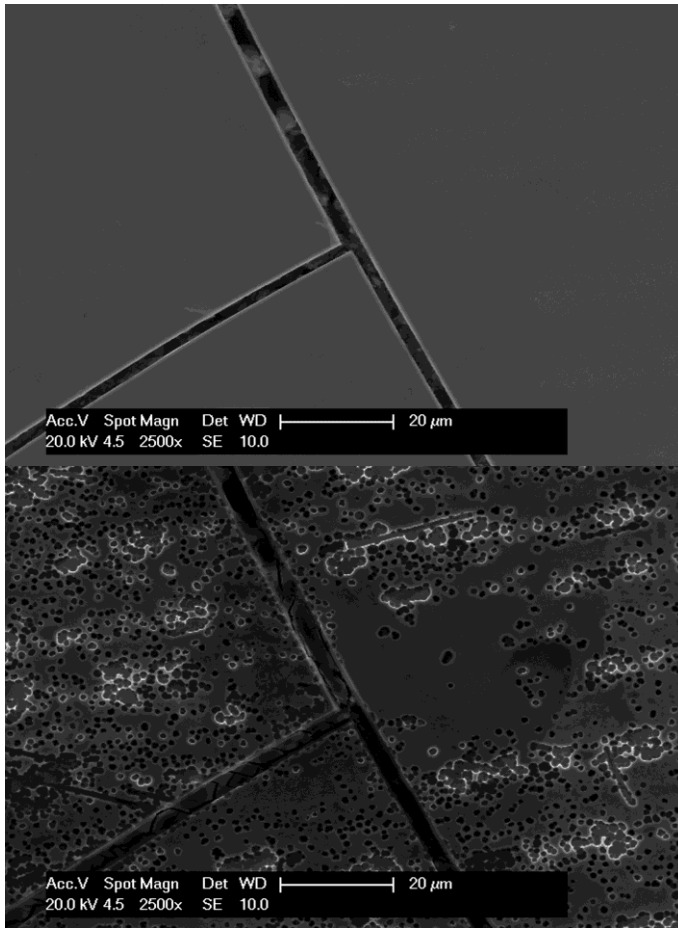
Figure 11: Surface morphology of a selected area of the laser treated amorphous sample before and after polarisation. (a) SE image before corrosion test in acid (b) SE image of the same area after corrosion test in acid.